# A 20-year study of melt processes over Larsen C Ice Shelf using a high-resolution regional atmospheric model: Part 1, Model configuration and validation

Ella M. K. Gilbert[1], Andrew Orr[1], John C. King[1], Ian Renfrew[2], and Tom A. Lachlan-Cope[1]

[1]British Antarctic Survey
[2]University of East Anglia

November 22, 2022

**Abstract**

Following collapses of the neighbouring Larsen A and B ice shelves, Larsen C has become a focus of increased attention. Determining how the prevailing meteorological conditions influence the surface melt regime is of paramount significance for understanding the dominant processes causing melt and ultimately for predicting its future. A new, high-resolution (4 km grid spacing) Met Office Unified Model (MetUM) hindcast of atmospheric conditions and surface melt processes over the central Antarctic Peninsula during the period 1998-2017 is developed for this purpose. The hindcast is capable of reliably simulating observed near-surface meteorology and surface melt conditions over Larsen C. In contrast with previous model simulations, the MetUM captures the observed east-west gradient in surface melting associated with foehn winds, as well as the inter-annual variability in melt shown in previous observational studies. The hindcast is applied to two case studies – the months preceding the collapse of the Larsen B ice shelf in March 2002 and the high-foehn, high-melt period of March-May 2016 - to test its ability to reproduce the atmospheric effects that contributed to considerable melting during those periods. The results suggest that the MetUM hindcast is a reliable tool with which to explore the dominant causes of surface melting on Larsen C.

# A 20-year study of melt processes over Larsen C Ice Shelf using a high-resolution regional atmospheric model: Part 1, Model configuration and validation

**E. Gilbert[1,2,] †, A. Orr[1], J. C. King[1], I. A. Renfrew[2] and T. Lachlan-Cope[2]**

[1] British Antarctic Survey, High Cross, Madingley Road, Cambridge CB3 0ET, United Kingdom.

[2] School of Environmental Sciences, University of East Anglia, Norwich NR4 7TJ, United Kingdom.

Corresponding author: Ella Gilbert (ella.gilbert@reading.ac.uk)

† Present address: Department of Meteorology, University of Reading, Whiteknights Road, Reading RG6 6ET, United Kingdom.

**Key words:** ice shelves; Antarctic Peninsula; regional climate modelling; surface melt; meteorology; model hindcast

**Key Points:**

- We present a new high-resolution, multi-decadal hindcast of atmospheric conditions and surface melt processes over the Larsen C ice shelf
- The model hindcast reliably captures the observed location, frequency and interannual variability of foehn events on Larsen C
- The hindcast captures the foehn-induced distribution and interannual variability of surface melt patterns on Larsen C

## Abstract

Following collapses of the neighbouring Larsen A and B ice shelves, Larsen C has become a focus of increased attention. Determining how the prevailing meteorological conditions influence the surface melt regime is of paramount significance for understanding the dominant processes causing melt and ultimately for predicting its future. A new, high-resolution (4 km grid spacing) Met Office Unified Model (MetUM) hindcast of atmospheric conditions and surface melt processes over the central Antarctic Peninsula during the period 1998-2017 is developed for this purpose. The hindcast is capable of reliably simulating observed near-surface meteorology and surface melt conditions over Larsen C. In contrast with previous model simulations, the MetUM captures the observed east-west gradient in surface melting associated with foehn winds, as well as the inter-annual variability in melt shown in previous observational studies. The hindcast is applied to two case studies – the months preceding the collapse of the Larsen B ice shelf in March 2002 and the high-foehn, high-melt period of March-May 2016 - to test its ability to reproduce the atmospheric effects that contributed to considerable melting during those periods. The results suggest that the MetUM hindcast is a reliable tool with which to explore the dominant causes of surface melting on Larsen C.



## Plain Language Summary

Scientists are concerned about floating ice shelves on the Antarctic Peninsula because several shelves have collapsed there in recent decades, due partly to melting at the surface. However, our understanding of what causes these ice shelves to melt is limited by the lack of observations in the region, and so numerical models are an extremely useful tool to explore this. This study showcases a new high-quality model dataset that is able of capturing the major patterns of surface melting and atmospheric conditions over ice shelves on the Antarctic Peninula. It represents an improvement on previous studies and can be reliably used to simulate melt and meteorology on ice shelves like Larsen C. The ability of the hindcast to capture these processes is tested by applying it to two case studies – the period just before the collapse of the Larsen B ice shelf in March 2002, and a period in March-May 2016 when exceptionally high melt and intense foehn winds were observed on the Larsen C ice shelf. This suggests that the hindcast is suitable for exploring the causes of ice shelf surface melting in the region.

## 1 Introduction

The Antarctic Peninsula has become a recent focus of attention because of the pace of environmental change there. Changes in the atmosphere and cryosphere have co-occurred: notably, surface warming of up to 3°C between 1951-2000 in the northern Antarctic Peninsula (Turner et al., 2016) has coincided with the loss of mass from more than half of the twelve ice shelves surrounding the Antarctic Peninsula since 1947, including the dramatic collapse of the Prince Gustav and Larsen A and B ice shelves (Cook & Vaughan, 2010). The loss or thinning of ice shelves contributes to sea level rise because their ability to buttress upstream grounded ice is reduced, accelerating tributary glaciers and hence the input of ice into the ocean (Rignot et al., 2004, Borstad et al., 2013; Trusel et al., 2015, Fürst et al., 2016).

The collapse of the Larsen A (in 1995) and B (in 2002) ice shelves on the east side of the Antarctic Peninsula was induced by hydrofracturing, whereby water-filled crevasses widen as a result of the hydrostatic pressure acting at the crevasse tip (Scambos et al., 2000; Kuipers Munneke, 2014). Surface melting is the most important driver of destabilisation via this mechanism because it triggers a series of glaciological processes that begins with firn densification (Scambos et al., 2000; van den Broeke, 2005; Holland et al., 2011). Surface meltwater percolates into the porous firn layer during summer, and once the firn becomes saturated with refrozen meltwater over many seasons, begins to collect in ponds on the surface because it cannot drain away (Scambos et al., 2000; Kuipers Munneke et al., 2014). This allows hydrofracturing to occur, leading to ice shelves disintegrating extremely rapidly: over about a month in the case of Larsen B (Scambos et al., 2003). The southward progression of ice shelf collapse on the east side of the Antarctic Peninsula indicates that Larsen C, the largest remaining ice shelf in this region, may become unstable in the near future (Rott et al., 1996; 2002; Scambos et al., 2003; Bevan et al., 2017).

Larsen C is located at approximately 66°S – 69°S and has an area of ~47,000 km2. Its climate is dominated by the influence of cold, continental air masses that flow off the Antarctic plateau as a southerly barrier jet (Parish, 1983). However, foehn winds, which are generated when air is forced over the steep terrain of the Antarctic Peninsula mountains, are also relatively frequently observed over Larsen C during periods of westerly and north-westerly flow, and these

dramatically alter the local climate and surface energy balance (SEB) for hours or days at a time (Cape et al., 2015; Elvidge et al., 2015; 2016; Elvidge & Renfrew, 2016; Kuipers Munneke et al., 2018; Elvidge et al., 2020). Luckman et al. (2014) and Bevan et al. (2018) used satellite measurements to show that annual meltwater production on Larsen C is highest in the north, where temperatures are closer to the melting point, and in inlets close to the mountains, where foehn winds are most intense and frequent (Turton et al., 2018; Elvidge et al., 2020). These foehn induced east-west gradients in melt are also seen in borehole and air content measurements that indicate firn densification in inlets (Hubbard et al., 2016; Bevan et al., 2017; Holland et al., 2011).

Foehn events are associated with both "jet" and "wake" regions over the Larsen C downwind of mountain passes, with the "jet" regions being relatively windier-but-cooler compared to the calmer-but-warmer "wake" regions (Elvidge et al.,2015; Elvidge et al., 2020). However, despite their importance for inducing melt over Larsen C, a reliable long-term estimate of how frequently foehn events occur and their associated impacts on SEB has not yet been made. Estimates of their frequency have been made only at single AWSs or locations on the ice shelf (Turton et al., 2018; Weisenekker et al., 2019) or over a relatively short time periods of a year or less (King et al., 2017; Kirchgaessner et al., 2019; Elvidge et al. 2020).

Regional climate models have been increasingly used in recent years to assess melting and near-surface meteorology on Larsen C. These models successfully simulate the temperature and solar radiation-driven north-south gradient in melting, but struggle to reproduce the east-west gradient in melt associated with foehn winds (e.g. van Wessem et al., 2016; Datta et al., 2019). This is largely a result of limitations in the modelling techniques used, such as insufficient horizontal resolution or restrictive numerical approximations when simulating the dynamics of foehn winds in complex orography, and therefore its impact on SEB, and consequently melting. For example, although Datta et al. (2018 & 2019) find enhanced surface melting and foehn occurrence in inlets on the southern part of Larsen C using the Modèle Atmosphérique Regionale at a spatial resolution of 10 and 7.5 km, it is only found in the strongest foehn cases, resulting in a much weaker east-west gradient in climatological melting than observed.

Recently Elvidge et al. (2020) using the UK Met Office Unified Model (MetUM) at a spatial resolution of 1.5 km became the first study to adequately capture the east-west gradient of foehn-driven melting on Larsen C and, importantly, to explain the drivers of melt in terms of boundary-layer processes affecting the SEB. However, the relatively short (6 month) period considered by that study promotes the need for a comprehensive and long-term (multi-decadal) model dataset that realistically includes the primary atmospheric processes contributing to the SEB and surface melt on Larsen C. This study will address this outstanding issue.

Firstly, and most importantly, a regional configuration of the MetUM at a spatial resolution of 4 km, which is able to resolve the foehn-driven melting over the Larsen ice shelves, will be presented and the output validated against automatic weather station (AWS) observations. Second, the ability of the MetUM to capture the observed spatial gradients and absolute totals of surface melting, and determine the dominant atmospheric drivers of these, will be examined. This will be done by evaluating surface melt and foehn occurrence over Larsen C during the main hindcast period 1998-2017, and by simulating two case studies: 1) the Larsen B ice shelf prior to its collapse in 2002, and 2) the Larsen C ice shelf during a concerted period of high melt / high foehn that occurred in 2016 (Kuipers-Munneke et al., 2018). In this paper, we present the first model-based multi-decadal climatological maps of surface melt and foehn occurrence for Larsen C. Note that analyses of these, including an evaluation of the primary causes of surface melt, will be developed further in a subsequent manuscript.

## 2 Data and Methods

### 2.1 Observational data

We use available AWS data from four stations, which are shown in Figure 1 and referred to as AWS 14, 15, 17, and 18. The longest record of any of the stations is from AWS 14, which covers the period January 2009 – December 2017, while AWSs 15, 17 and 18 cover the periods January 2009 – June 2014, February 2011 – March 2016 and November 2014 – December 2017, respectively. AWS 14 and 15 are both located on a flat and homogeneous region of the Larsen C ice shelf, meaning that measurements taken at these stations are representative of a wider area, as demonstrated in King et al. (2015). Conversely, both AWS 17 and 18 are located in inlets at the

base of steep topography, where the meteorology is highly localised. AWS 17 sits on the remnant Larsen B ice shelf, in Scar Inlet, while AWS 18 is located in Cabinet Inlet, close to the foot of the mountains in the north-west of the Larsen C ice shelf.

All stations measure the near-surface meteorology and we then derive the full SEB, although turbulent flux estimates were not available from AWS 15 at the time of analysis. The instrumentation used at the AWSs is described in detail in Kuipers Munneke et al. (2012). The turbulent fluxes are calculated using the bulk method, by applying the SEB model of Kuipers Munneke et al. (2009). Corrections are made to the unventilated temperature data to adjust for positive biases in calm, sunny conditions after Smeets (2006) and Smeets et al. (2018), while shortwave fluxes are corrected for the tilt of the sensor according to the routine of Wang et al. (2016).

The SEB is formulated as follows:

$$E_{tot} = LW_{\uparrow} + LW_{\downarrow} + SW_{\uparrow} + SW_{\downarrow} + H_S + H_L + G_S \quad (1)$$

where $E_{tot}$ is the net sum of energy received at the surface, $LW_{\uparrow}$ and $LW_{\downarrow}$ are the upwelling and downwelling components of LW radiation, respectively, $SW_{\uparrow}$ and $SW_{\downarrow}$ are the upwelling and downwelling components of SW radiation, respectively, and $H_S$, $H_L$ and $G_S$ are the surface sensible, latent and ground heat fluxes, respectively. All fluxes are defined as positive when directed towards the surface.

Surface melt energy $E_{melt}$ is defined as in King et al. (2015), as:

$$E_{melt} = \begin{cases} E_{tot} & T_S \geq 0°\mathrm{C} \\ 0 & T_S < 0°\mathrm{C} \end{cases} \quad (2)$$

such that melt only occurs when there is a surplus of energy at the surface ($E_{tot}$ in Equation 1 is positive) and the surface temperature, $T_S$, is at or above the melting point.

### 2.2 Regional climate model description

In this study the MetUM is run in a high-resolution atmosphere-only limited area configuration. The MetUM contains a non-hydrostatic, fully compressible dynamical core, referred to as

ENDGAME (Even Newer Dynamics for General Atmosphere Modelling of the Environment), with semi-implicit time stepping and semi-Lagrangian advection. Atmospheric prognostic variables are the dry virtual potential temperature, Exner pressure, dry density and three-dimensional winds, and moist prognostics such as hydrometeors and specific humidity are advected as atmospheric tracers (Walters et al., 2017). Prognostic variables are discretised horizontally on an Arakawa-C grid and a terrain-following hybrid vertical coordinate with Charney-Phillips staggering used in the vertical.

An inner model domain that includes much of the Antarctic Peninsula and surrounding waters (Figure 1) is nested within a global version of the MetUM to dynamically downscale the global model output to higher resolution, as in Orr et al. (2014) and Gilbert et al. (2020). The global model is run using Global Atmosphere 6.1 physics (Walters et al., 2017) and has N768 resolution (equivalent to a horizontal resolution of approximately 17 km at mid-latitudes). The inner domain has 70 vertical levels (with 40 below 5500 m), and uses a rotated latitude-longitude grid to maintain uniform horizontal resolution of 4.0 km. Although Elvidge et al. (2015) argued that a horizontal grid spacing of around 1.5 km was necessary to resolve foehn winds over Larsen C, this argument was based on the previous version of the dynamical core. Recent improvements incorporated in ENDGAME (Wood et al., 2014) have resulted in a more accurate representation of the flow response to orography, meaning a spatial resolution of ~4 km is now sufficient (Gilbert et al., 2020).

The inner domain runs using the Regional Atmosphere (RA) configuration 'RA1M' physics package described in Bush et al. (2020), with modifications to the parameterisation of large-scale cloud and precipitation as described in Gilbert et al. (2020). Gilbert et al. (2020) showed that this was the optimum model configuration currently available for this region and recommended that it be used for further work examining SEB and melt. Full details of the model physics and parameterisations used are given in Gilbert et al. (2020).

Because of the important influence of the mountains (and land-sea interactions – see Orr et al. (2005, 2014)), the default model orography and coastline were updated using better resolved datasets. The updated land-sea mask is based on the Scientific Committee on Antarctic Research Antarctic Digital Database coastline, version 7.0 (released January 2016 and available at

https://www.add.scar.org/). The orography is based on the Ohio State University Radarsat Antarctic Mapping Project (RAMP) 200 m resolution Antarctic digital elevation model (Liu, 2015), and is converted for use in the MetUM by interpolating the dataset onto the 4.0 km inner domain and applying a 2D 1-2-1 filter with convolution.

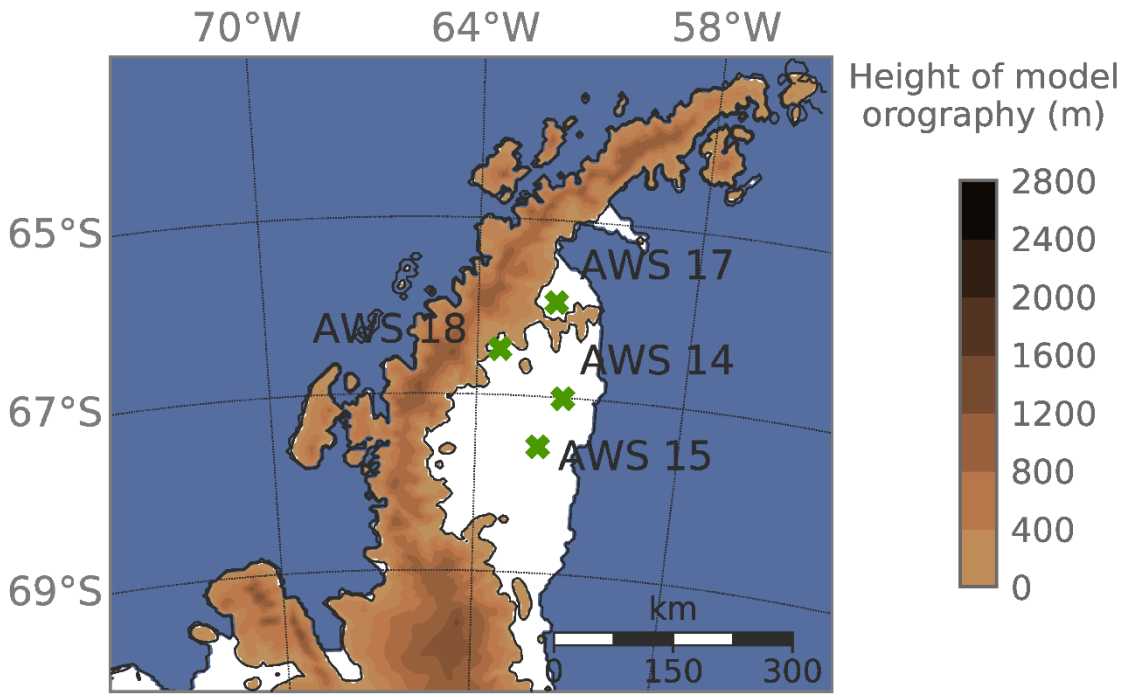


**Figure 1**. Map of the Antarctic Peninsula MetUM inner model domain at a spatial resolution of 4 km, with the locations of the four AWSs used for validation indicated with green crosses. The map is centred on the Larsen C ice shelf and its tributary inlets, on which AWS 14, 15 and 17 are located. The map also shows the remnant Larsen B ice shelf on which AWS 17 is located. The height of the model orography is indicated with coloured contours and is derived from the RAMP 200 m elevation model (Liu, 2015). Ice shelves are shown in white.

### 2.3 Method

The MetUM is primarily used to produce a model hindcast of the northern and central Antarctic Peninsula and Larsen C region over the period 1 January 1998 to 31 December 2017. An additional shorter run is also undertaken to focus on the conditions over Larsen B prior to its

collapse. This case study spans the period 1 September 2001 – 31 March 2002 and uses a modified land-sea mask that includes both the Larsen A and B ice shelves.

In both the 20-year hindcast and shorter case study runs, the global model is initialised from ERA-Interim reanalysis (Dee et al., 2011), and its output is used to provide forcing for the regional climate model / inner domain at 4.0 km horizontal resolution (Figure 1). The model is re-initialised every 12 hours and runs for 24 hours. The first 12-hour periods are considered spin-ups and discarded; while the second 12-hour periods are concatenated together to produce a continuous time series spanning the period of interest. Frequent re-initialisation ensures that the circulation in the inner domain is well constrained and does not drift (Sedlar et al., 2020; Lo et al., 2008), while the discarding of spin-up periods ensures that smaller-scale features are adequately represented. Surface (2D) variables are outputted 3-hourly and 3D variables are 6-hourly, which is considered sufficient temporal resolution to capture key processes such as foehn. A full list of output variables is given in the appendix.

The occurrence of foehn winds in the model is calculated using two methods that vary in computational expense. To compute the occurrence of model foehn winds at grid points corresponding to AWSs (Tables 3 and 4), an isentrope-based method adapted from the broad-scale approach of King et al. (2017) is adopted, with an additional stipulation that surface warming and/or drying must also be simulated. Whereas King et al. diagnose foehn occurrence across the ice shelf as a whole, in this study the algorithm is used to detect foehn occurrence at each model grid cell. The algorithm is as follows:

- Determine the strength of the westerly component of the wind, u , at a location at least one Rossby radius of deformation, $\lambda R$, westwards / upwind of the Antarctic Peninsula. $\lambda R$ is calculated as $\lambda R = Nh/f$, where N is the Brunt-Väisälä frequency, typically 0.01 $s^{-1}$, h is the height of the mountain barrier, approximately 1500-2000 m on the Antarctic Peninsula, and f is the Coriolis parameter. The wind is averaged between 250 m and a height Z1 in a manner similar to Elvidge et al. (2015) and referred to as $u_{Z1}$, where Z1 is just above the peak height of orography, i.e. it is characteristic of the average westerly

flow impinging on the Antarctic Peninsula. If $u_{Z1} \geq 2$ m $s^{-1}$ (and there is therefore a clear west-east cross-barrier flow) then for each model grid point:

- Find the potential temperature at Z1, $\theta_{Z1}$, and trace this isentrope directly eastwards across the mountain barrier
- Determine the minimum elevation, Z2, of $\theta_{Z1}$ on the lee side of the mountains over Larsen C
- Determine the maximum change in height of the isentrope $\theta_{Z1}$ upwind and downwind of the barrier, i.e. Z3 = Z1 – Z2.
- For a model grid point, if over any 6 hour period Z3 > 500 m AND 1.5 m air temperature, Tair, increases AND 1.5 m relative humidity, RH, decreases, then foehn conditions are detected.

As this approach is extremely computationally expensive it cannot be used for every grid point in the model domain. Hence, to produce spatial maps of foehn occurrence over the entire Larsen C ice shelf, the method of Turton et al. (2018) was adapted. Turton et al. detect foehn conditions when, over a 12-hour period, one of the following conditions is met:

a) Decrease in relative humidity, RH, below the 10th percentile
b) Decrease in RH below a location-specific threshold
c) Decrease in RH below the 15th percentile plus a 3°C increase in $T_{air}$

We adopt conditions a) and c), plus include a further stipulation that there be a westerly wind component ($u_{Z1} > 2.0$ m $s^{-1}$), as above. Sensitivity tests (not shown) showed that the two methods of identifying foehn events produced comparable results.

## 3 Results and Discussion

### 3.1 Model hindcast validation

The MetUM hindcast is validated at all AWSs shown in Figure 1 using all available observations and taking the closest model gridpoint to each AWS. Missing data are linearly interpolated for validation purposes. Initial inspection of time series at each station (not shown), reveals that AWS 17/18 and AWS 14/15 are similar enough to justify being grouped. The means of the time series at AWS 14/15 and AWS 17/18 are hereafter presented as "ice shelf" and "inlet" stations,

respectively. Because the full SEB was not available at AWS 15, ice shelf values for $T_S$, $H_L$, $H_S$, $E_{tot}$ and $E_{melt}$ are taken from AWS 14 only. The full SEB is available at both inlet stations. Table 1 shows observed and modelled annual mean values and the 5th and 95th percentiles for surface variables at inlet and ice shelf stations during the hindcast period. Observed and modelled statistics in Table 1 are given for the observational period available for each station. Scatterplots of observed vs. modelled near-surface variables at AWS 14 during the entire observational period for that station (January 2009 - December 2017) are shown in Figure 2. Validation results at all stations are broadly similar to those for AWS 14, so for brevity, only results from AWS 14 are shown in Figure 2 because it has the longest observational record. These are discussed below.

As also shown by Kuipers Munneke et al. (2018), Gilbert et al. (2020) and Elvidge et al. (2020), the MetUM model at a spatial resolution of 4 km or finer is able to reliably simulate meteorological conditions and consequently the SEB and surface melt over Larsen C in all seasons. This is confirmed by both Figure 2 and Table 1. As shown in Table 1, annual mean $T_{air}$, $T_S$, wind speed and relative humidity are positively biased by 2.1°C, 2.4°C, 0.91 m $s^{-1}$ and 2.7%, respectively, at inlet stations and 2.1°C, 3.1°C, 0.81 m $s^{-1}$ and 3.8%, respectively, at ice shelf stations. This makes the MetUM hindcast on average slightly warmer, windier and moister than observations, which is also clear from Figure 2.

The warm bias in air and surface temperatures is likely at least partially related to the representation of boundary layer mixing in the MetUM and a documented warm bias in ERA-Interim (Fréville et al., 2014; Dutra et al., 2015). Because $T_{air}$ and $T_S$ are biased by different amounts, the near-surface temperature gradient is too small, which contributes to biases in $H_S$. Wind and relative humidity biases may be related to the representation of features and processes such as orography, form drag and surface roughness (Wood & Mason, 1993), the representation of foehn events and foehn jets, the surface and snow schemes, or the influence of the coastline (Orr et al., 2005; 2014). Additionally, the seasonal cycle and timing of weather events in the MetUM hindcast (not shown) matches well between model and observations, which produces high correlation coefficients (Figure 2) and low RMSEs for most parameters in Table 1.

The inter-percentile range for most variables in Table 1 is captured relatively well by the hindcast, except for relative humidity and $H_S$. The 5th percentile of observed relative humidity

and the 95th percentile of $H_S$ are much lower and higher, respectively, at inlet stations than ice shelf stations due to the effect of foehn winds. However, the hindcast does not capture this completely: the 5th percentile of modelled inlet relative humidity is over-estimated by 7.9% while the 95th percentile of HS is 7.1 W $m^{-2}$ too large in the model. This is likely caused by the positive temperature bias shown in Table 1.

In Table 1 the annual mean downwelling radiative fluxes are simulated to within 10% of their observed values at all stations and the model SW albedo ($SW_{\downarrow}/SW_{\uparrow}$) is simulated to within 1% and 3% of observed values at inlet and ice shelf stations, respectively. Positive biases in $T_S$ and Tair cause $LW_{\uparrow}$ to be over-estimated by 2.9% annually at all stations, generating an energy deficit at the surface (and negatively biased mean net radiation $R_{net}$, (calculated as $LW_{net}$ + $SW_{net}$), shown in Figure 2). This causes annual mean daily mean $E_{melt}$ to be under-estimated by 17-31%, particularly at inlet stations.

Negative $E_{melt}$ biases are largest during December-February (DJF, not shown) when the majority of melting occurs, and during foehn events. These biases in $E_{melt}$ during foehn events, and the HS and relative humidity biases noted above, are consistent with previous findings that the MetUM under-predicts the magnitude of foehn-driven $E_{melt}$ fluxes. For example Gilbert (2020) found that although the MetUM was able to capture the timing and duration of the foehn cases examined, the magnitude of $E_{melt}$ was under-estimated. To summarise, at all stations and in all seasons, the hindcast is able to simulate observed surface meteorological variables reliably and to broadly capture SEB components, although $E_{melt}$ is under-estimated. Most of the biases in SEB terms stem from a warm temperature bias.

**Table 1.** Summary statistics for inlet and ice shelf stations in observations and model output. Mean values, as well as the fifth and ninety-fifth percentiles of daily mean surface variables are given, where abbreviations and units are as follows: $T_S$: surface temperature (°C); $T_{air}$: 1.5 m air temperature (°C); RH: relative humidity (%), FF: 10 m wind speed (m $s^{-1}$); P: surface pressure (hPa); $SW_{\downarrow}$: downwelling shortwave radiation (W $m^{-2}$), $SW_{\uparrow}$: upwelling shortwave radiation (W $m^{-2}$); $SW_{net}$: net shortwave radiation (W $m^{-2}$); $LW_{\downarrow}$: downwelling shortwave radiation (W $m^{-2}$); $LW_{\uparrow}$: upwelling shortwave radiation (W $m^{-2}$); $LW_{net}$: net shortwave radiation (W $m^{-2}$); $H_S$: sensible heat flux (W $m^{-2}$); $H_L$: latent heat flux (W $m^{-2}$); $E_{tot}$: sum of all (W $m^{-2}$); $E_{melt}$: melt flux (W $m^{-2}$). All fluxes are positive when directed towards the surface.

| | Observed | | | | | | Modelled | | | | | |
|---|---|---|---|---|---|---|---|---|---|---|---|---|
| | Ice shelf | | | Inlet | | | Ice shelf | | | Inlet | | |
| | **Mean** | **5th** | **95th** | **Mean** | **5th** | **95th** | **Mean** | **5th** | **95th** | **Mean** | **5th** | **95th** |
| $T_{air}$ | -15.4 | -32.1 | -1.5 | -14.0 | -30.1 | 0.3 | -12.2 | -25.7 | -1.4 | -11.9 | -24.9 | -1.1 |
| $T_S$ | -14.9 | -31.5 | -1.2 | -14.4 | -30.4 | -1.1 | -12.7 | -26.6 | -1.5 | -12.8 | -26.1 | -1.7 |
| $FF$ | 4.2 | 1.1 | 9.2 | 4.2 | 1.0 | 11.2 | 5.2 | 2.4 | 10.1 | 5.3 | 1.8 | 12.1 |
| $P$ | 985.0 | 966.4 | 1003.9 | 984.5 | 965.0 | 1004.1 | 983.4 | 965.0 | 1002.3 | 983.0 | 964.0 | 1001.7 |
| $RH$ | 93.1 | 80.2 | 100.0 | 91.1 | 65.6 | 99.1 | 97.2 | 83.6 | 109.0 | 93.6 | 73.5 | 107.3 |
| $SW_{\downarrow}$ | 128.2 | 0.3 | 345.5 | 126.9 | 1.3 | 332.8 | 124.9 | 0.0 | 357.6 | 124.1 | 0.0 | 365.7 |
| $SW_{\uparrow}$ | -111.5 | -0.1 | -289.8 | -107.7 | -1.2 | -276.2 | -105.1 | -292.4 | 0.0 | -104.1 | -297.1 | 0.0 |
| $SW_{net}$ | -18.7 | 0.0 | -63.5 | -19.2 | -0.1 | -64.4 | -19.8 | 0.0 | -65.8 | -20.0 | 0.0 | -68.4 |
| $LW_{\downarrow}$ | 236.1 | 181.0 | 295.9 | 237.8 | 185.7 | 293.9 | 234.0 | 162.7 | 298.3 | 231.5 | 167.5 | 293.3 |
| $LW_{\uparrow}$ | -254.5 | -193.6 | -310.3 | -256.5 | -197.0 | -310.5 | -262.5 | -308.6 | -209.3 | -261.8 | -307.8 | -211.0 |
| $LW_{net}$ | -15.7 | -47.3 | 1.2 | -18.6 | -53.5 | 1.3 | -28.5 | -68.3 | 0.7 | -30.3 | -66.9 | -2.1 |
| $H_S$ | -0.9 | -14.8 | 22.6 | 3.4 | -13.1 | 47.4 | 4.0 | -11.3 | 34.3 | 7.2 | -10.7 | 54.5 |
| $H_L$ | -3.2 | -14.0 | 2.0 | -4.2 | -14.9 | 0.9 | -1.8 | -11.6 | 4.6 | -3.8 | -15.2 | 2.3 |
| $E_{tot}$ | -3.4 | -28.4 | 24.5 | -3.4 | -29.1 | 26.3 | -6.5 | -35.3 | 18.7 | -6.9 | -33.7 | 20.2 |
| $E_{melt}$ | 2.7 | 0.0 | 19.8 | 3.4 | 0.0 | 24.2 | 1.8 | 0.0 | 13.2 | 2.4 | 0.0 | 15.8 |

342
343
344

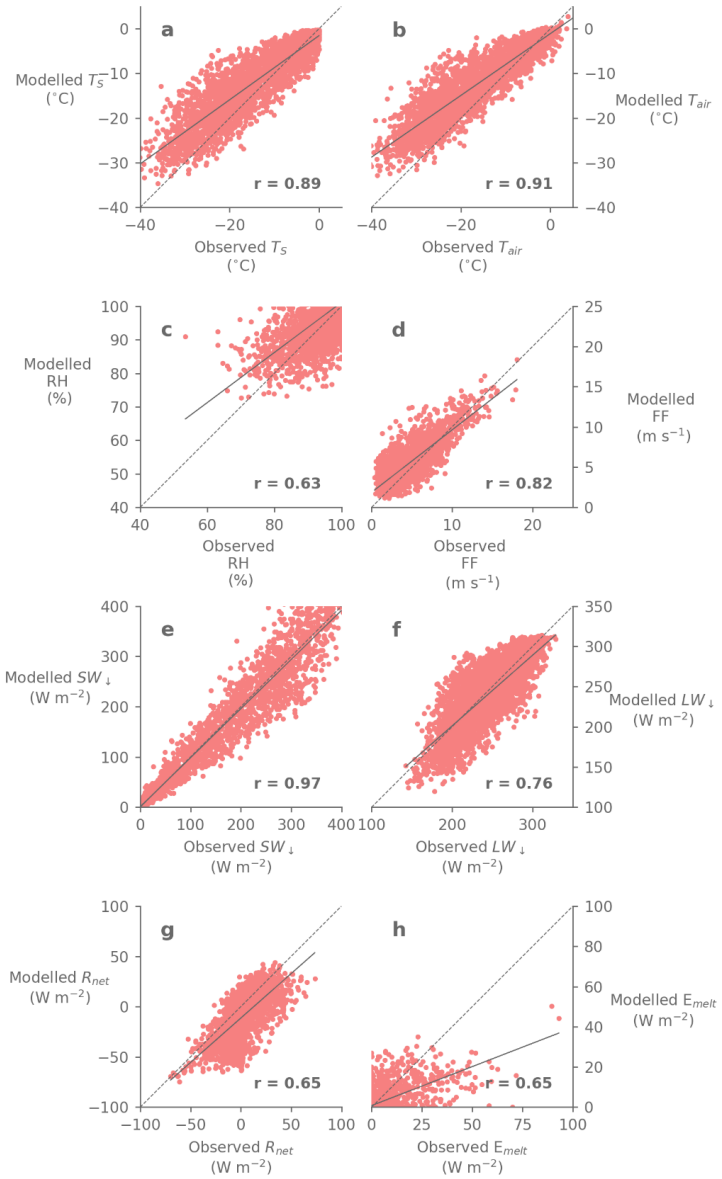


**Figure 2**. Scatterplots of observed vs. modelled daily means of surface and near-surface variables at AWS 14. Correlation coefficients (r values) are given in the bottom right-hand corner of each panel: all values are statistically significant at the 99% level. The dashed line in each plot indicates perfect agreement between model and observations, while the solid line shows the line of best fit, calculated by a linear least-squares regression. Panels a – d show surface meteorological variables: surface temperature, $T_S$; near-surface (1.5 m) air temperature, $T_{air}$; 1.5 m relative humidity; and 10 m wind speed; and panels e – h show surface energy budget terms: downwelling longwave, $LW_\downarrow$; downwelling shortwave, $SW_\downarrow$; net radiative, $R_{net}$ and melt, $E_{melt}$, fluxes, defined as positive towards the surface.

### 3.2 Modelled meltwater production: Larsen C, from 1998 to 2017

Figure 3 shows cumulative annual simulated meltwater production for all full melt years included in the hindcast period (a total of 19 melt years, starting August 1998 and ending July 2017), where melt years are defined as in Bevan et al. (2018) from August-July. This is the first spatial map of mean surface meltwater production on Larsen C derived from a multi-year model simulation. Table 2. contains mean and maximum cumulative annual melt totals for the whole Larsen C ice shelf and shows that mean cumulative melt ranges from 86 mm w.e. $yr^{-1}$ in 2010/11 to 188 mm w.e. $yr^{-1}$ in 2006/07, with maxima simulated in inlets peaking at 1025 mm w.e. $yr^{-1}$ in 2016/17.

The simulated spatial pattern of meltwater production (Figure 3) is consistent with satellite observations of surface melting (e.g. Bevan et al., 2018; Luckman et al., 2014), with a clear north-south gradient across the ice shelf, and more melting observed in inlets. The hindcast also simulates peak mean meltwater production during the high melt years identified in Bevan et al. (2018), for example the 1998/99, 2006/07, 2015/16 and 2016/17 melt seasons, when ice-shelf averaged cumulative annual melt of 117 mm w.e., 187 mm w.e., 157 mm w.e. and 161 mm w.e., respectively, is modelled. The spatial patterns of surface melt shown in Bevan et al. (their Figure 6) are quite closely reproduced in Figure 3, for example more intense melting in inlets during 2015/16, 2016/17 and 2013/14 is successfully reproduced, as are the relatively low melt years of 2009/10, 2010/11 and 2014/15. Years where melt is shown in satellite observations but not the hindcast include 2001/02 and 2002/03, and the hindcast simulates more melt during 2006/07 than is shown in Bevan et al. (2018). Overall, however, the model's ability to reproduce the major patterns of melting, particularly the east-west gradient and concentration of meltwater production in inlets and the slopes immediately above is extremely encouraging and further justifies the use of the MetUM as a tool for studying this region.

Simulated mean annual meltwater production amounts over Larsen C (Figure 3, Table 2) are also comparable to those derived by Trusel et al. (2013), who used satellite data and modelling to find ice-shelf integrated mean meltwater production of 220 mm w.e. $yr^{-1}$ over the period 1999-2009, exceeding 400 mm w.e. $yr^{-1}$ in the north-western inlets, and Trusel et al. (2015) who show contemporary melt rates over Larsen C of ~300 mm w.e. $yr^{-1}$. Comparable hindcast-simulated

values for 1998-2017 are 132 mm w.e. $yr^{-1}$ for all of Larsen C, and 536 mm w.e. $yr^{-1}$ for inlets only, taking maximum meltwater production rates as a proxy for inlet melting (maxima are always observed in inlets). This suggests that the MetUM may under-estimate surface melting when averaged across the whole ice shelf, consistent with the results shown in Section 3.1. Although the ice-shelf-mean meltwater totals do not compare exactly in absolute terms with the satellite-based observations, the distributions do compare well. Further, it is notable that maximum values simulated in the north-western inlets during high melt years (up to 797 mm w.e., 602mm w.e. and 1025 mm w.e. in Mill Inlet, on the south-west of Larsen C, during 2013/14, 2015/16 and 2016/17, respectively, and up to 780 mm w.e. in Cabinet Inlet (the location of AWS 18), in the north-west, during 2006/07) exceed the ~725 mm w.e $yr^{-1}$ observed over Larsen B before its collapse (Trusel et al., 2015).

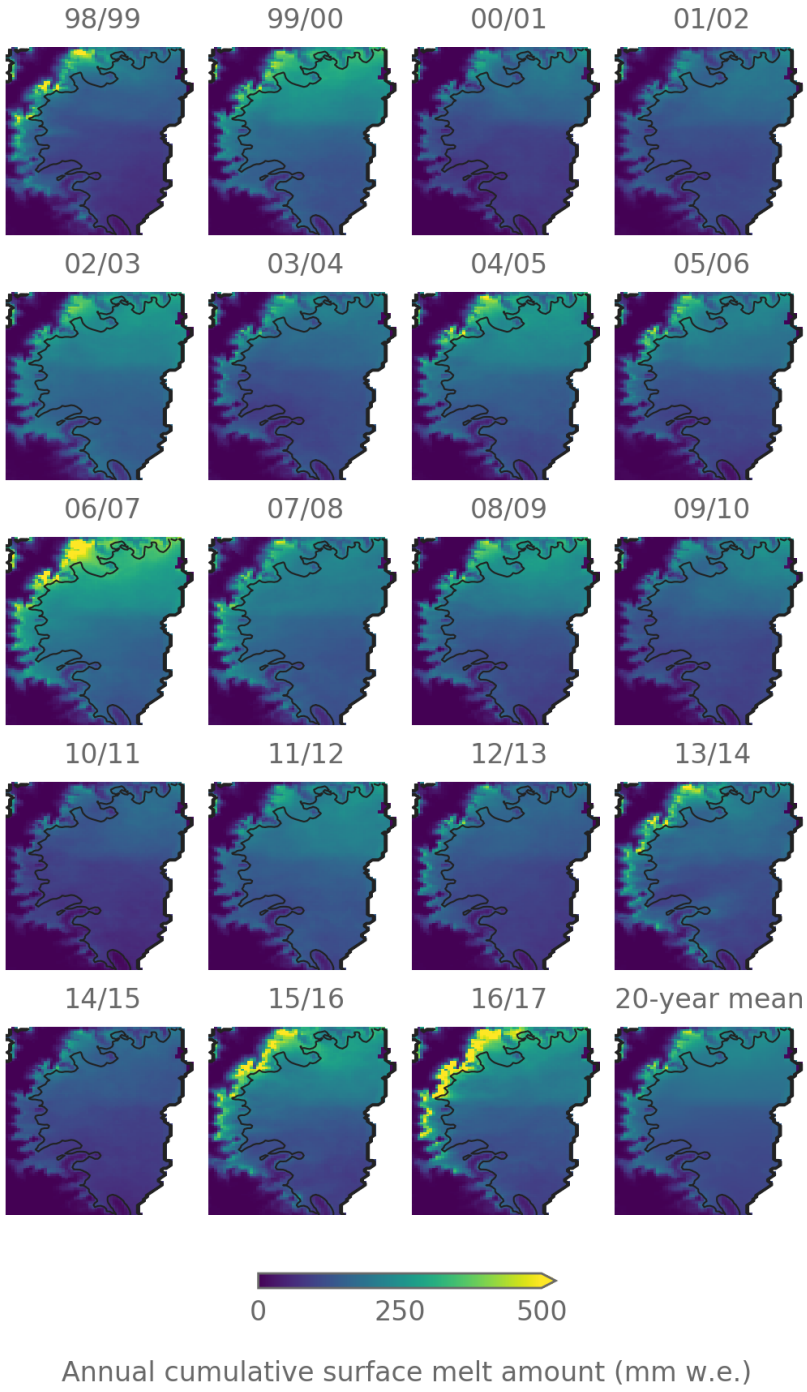


396 **Figure 3.** Total annual cumulative snow melt amount (in mm meltwater equivalent per year, mm
397 w.e. $yr^{-1}$) across the Larsen C ice shelf for each melt year (August - July, defined as in Luckman
398 et al., 2014 and Bevan et al., 2018) in the period 1998-2017. The 50 m elevation contour is
399 given, approximately the height of the modelled ice shelf at the grounding line. The bottom right
400 subplot shows the mean annual cumulative snow melt amount for all melt seasons.

**Table 2.** Total and maximum modelled meltwater production over the Larsen C ice shelf and tributary glaciers during each melt year (August-July) in the hindcast period. Annual ice shelf-integrated and maximum modelled meltwater production greater than one standard deviation above the mean are indicated with bold underlined text, while modelled meltwater production less than one standard deviation below the mean is indicated with italic underlined text. The mean and standard deviation ("SD") are shown in the bottom two rows.

| **Melt year** | **Ice shelf mean annual total meltwater production (mm w.e.)** | **Maximum annual total meltwater production (mm w.e.)** |
|---|---|---|
| 98-99 | 117 | 762 |
| 99-00 | 157 | 488 |
| 00-01 | *99* | 422 |
| 01-02 | 111 | 439 |
| 02-03 | 156 | 414 |
| 03-04 | 118 | 420 |
| 04-05 | 146 | 574 |
| 05-06 | 125 | 467 |
| 06-07 | **188** | **780** |
| 07-08 | 149 | 482 |
| 08-09 | 136 | 451 |
| 09-10 | 113 | 397 |
| 10-11 | *86* | 370 |
| 11-12 | 131 | 411 |
| 12-13 | *103* | 421 |
| 13-14 | 131 | 602 |
| 14-15 | *94* | 347 |
| 15-16 | **157** | **797** |
| 16-17 | **161** | **1025** |
| **Mean** | 130 | 530 |
| **SD** | 26 | 178 |

### 3.3 Modelled meltwater production: The 2001/02 melt season, prior to the break-up of Larsen B

Having established that the MetUM is able to realistically simulate the magnitude and spatial patterns of surface melting observed on the Larsen C ice shelf, we now consider as a case study the period immediately preceding the collapse of Larsen B. Figure 4 shows the cumulative melt amount simulated over the seven-month time period prior to Larsen B's collapse, from the additional shorter run for the period 1 September 2001 – 31 March 2002 (with the Larsen B ice shelf still intact). Mean cumulative surface melt of 340 mm w.e. is modelled across the Larsen B ice shelf during 1 September - 15 February, peaking at 664 mm w.e. in the foot of the mountains (Figure 4). This magnitude of melt is comparable to the value of ~725 mm w.e. $yr^{-1}$ reported by Trusel et al. (2015) to have been observed prior to its collapse. Particularly, melting in inlets close to the grounding line (approximately in the vicinity of the 50 m elevation contour given in Figure 4) could have destabilised the ice shelf in a critical area. Melt-induced thinning in the vicinity of the grounding line has been shown to reduce ice shelf buttressing capacity more considerably than elsewhere on the shelf (Khazendar et al., 2016).

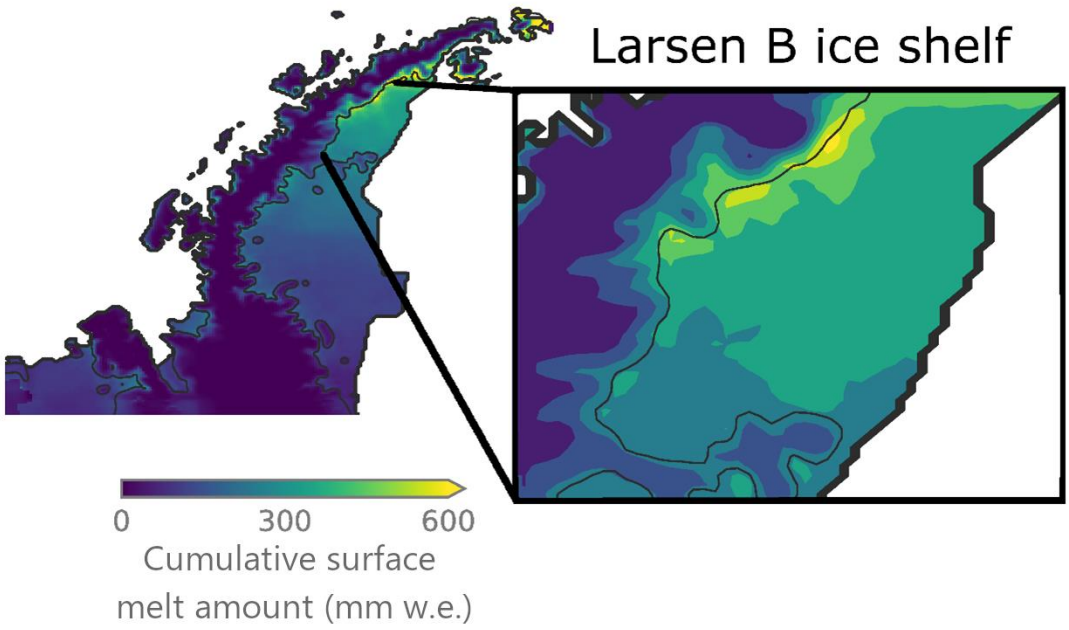


**Figure 4**. Cumulative surface melt amount simulated during the period 1 September 2001 – 15 February 2002 over the Antarctic Peninsula domain (with the Larsen B ice shelf still intact, main figure) and zoomed in over the Larsen B ice shelf only (inset). The 50 m elevation contour is shown in both plots as the black contour.

The ability of this model run to capture the causes of this extensive melting are next examined. In the simulation, the majority of melting occurred mid-November - February, with sustained daily mean modelled ice-shelf melt fluxes and meltwater production of 8.4 W $m^{-2}$ and 2.2 mm w.e., respectively. Van den Broeke (2005) reports that the 2001/02 melt season was three times longer than the average of the preceding five summers because of the synoptic conditions, which established anomalously low sea ice concentrations in the Weddell Sea (east of Larsen B) and strong foehn flow. Figure 5a shows the mean modelled meteorological conditions across the entire Antarctic Peninsula domain, and over Larsen B (Figure 5b) during the period 10 November 2001 – 1 March 2002. During this period, the melt point was frequently reached (not shown), allowing melting to occur, especially in a narrow band along the foot of the mountains in the northwest of the ice shelf, where $T_{max}$ was also frequently above 0°C (Figure 5b).

Low wind speeds (<3 m $s^{-1}$) over Larsen B and strong upwind westerly flow caused by an anomalously deep Amundsen Sea Low suggests that foehn were important in producing higher surface melt fluxes. This is also suggested by Cape et al. (2015), who show a strong correlation between the monthly mean number of melt days and monthly mean foehn frequency anomaly over Larsen B during this period, and is further supported by the positive and negative mean $H_L$ and $H_S$, respectively, shown in Figure 5c and 5d. Large negative and positive $H_L$ and $H_S$ fluxes of the order of 100s W $m^{-2}$, respectively, are simulated in the lee of mountains upstream of Larsen B, suggesting an influx of warmer, drier air produced by foehn flow. During this period, this generates mean $E_{tot}$ fluxes averaged across Larsen B of 2.0 W $m^{-2}$, driving melt whenever surface temperatures exceed the melting point.

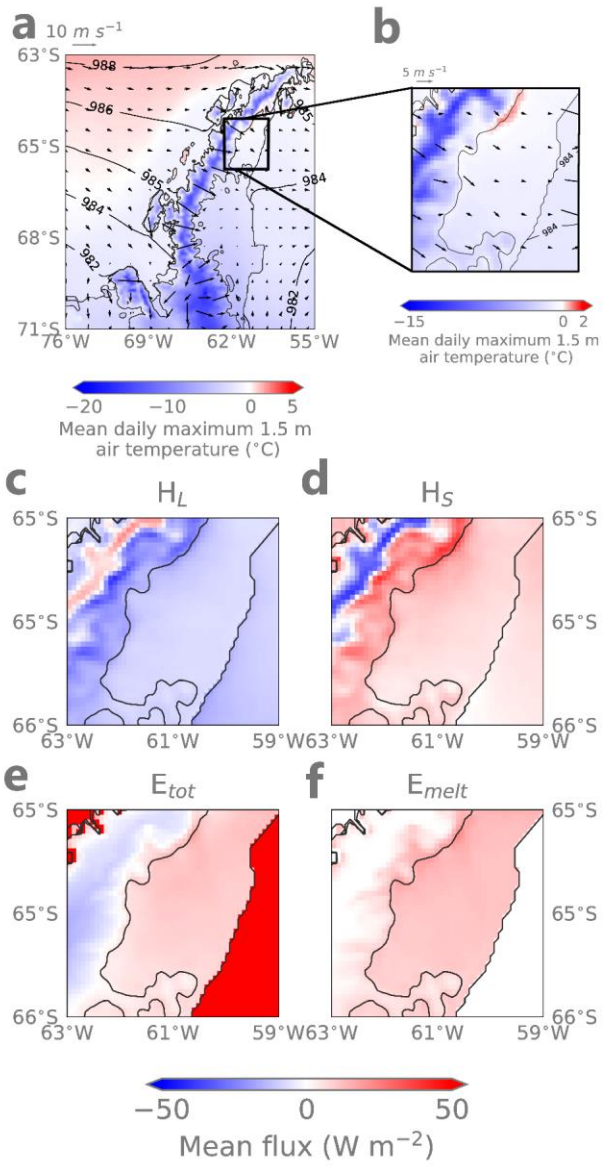


**Figure 5**. Mean modelled synoptic meteorological conditions and SEB components during 10 November 2001 - 1 March 2002, when melt was occurring. Panels a) and b) show mean meteorological conditions, where coloured shading shows the mean daily maximum 1.5 m air temperature throughout this period, and contours and vectors give mean sea level pressure and 10 m winds, respectively. Note that the land-sea mask includes the Larsen A and B ice shelves. Mean conditions are shown in panel a) while the inset (panel b) shows conditions over the Larsen B ice shelf only. Note that the temperature and wind speed scales are altered in the inset to show more detail. Panels c) - f) show mean surface energy fluxes ($H_L$, $H_S$, $E_{tot}$ and $E_{melt}$, respectively) over the Larsen B ice shelf, in units of W $m^{-2}$.

### 3.4 Frequency of foehn events: Larsen C, from 1998 to 2017

The frequency of foehn events at inlet and ice shelf stations is diagnosed using the isentrope-based method detailed in Section 2.3. Table 3 shows summary statistics (mean, median and standard deviations) of foehn occurrence at inlet and ice shelf stations for the hindcast period, decomposed into seasons, and given as an annual average. The modelled spatial distribution of foehn occurrence across the Larsen C ice shelf is shown in Figure 4, computed using the method of Turton et al. (2018) detailed in Section 2.3.

Consistent with previous studies (e.g. Turton et al., 2018; Wiesennekker et al., 2018; Datta et al., 2019; Elvidge et al., 2020) the highest foehn frequencies are simulated in the immediate lee of steep elevation, with foehn events occurring on average 16% of the time annually at inlet stations and 13% of the time at ice shelf stations (Figure 6, Table 3), comparable values to those cited in the aforementioned studies. A clear gradient is evident in Figure 6 with foehn frequency declining with distance from the mountains. The gradient is qualitatively similar to the gradient in surface melting shown in Figure 3, with higher melt simulated in the northwest and in inlets, suggesting a contributory role for foehn in causing surface melt. The importance of foehn in driving melt will be evaluated in Part 2 of this study. Foehn events are most common during September-November (SON) at all locations and standard deviations are highest in December-February (DJF) and MAM, indicating higher inter-annual variability in foehn occurrence in these seasons (Table 3). In recent years, unusually high foehn-driven surface melting has been reported in non-summer seasons, particularly MAM 2016 (Kuipers Munneke et al., 2018), which is discussed in detail next.

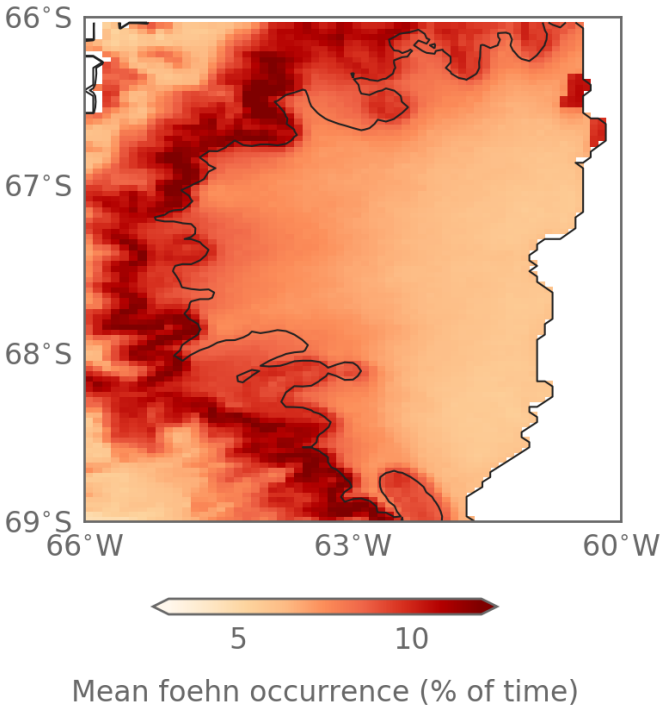


**Figure 6**. Annual modelled foehn occurrence and melt duration over the Larsen C ice shelf for the hindcast period. Foehn occurrence is shown as the mean percentage of time over the period 1998-2017 where foehn conditions are diagnosed over Larsen C, using the surface-based foehn diagnosis method of Turton et al. (2018) with an additional requirement, as in King et al. (2017), that there be a westerly wind component ($u_{Z1} > 2.0$ m $s^{-1}$). See methods for more details.

**Table 3.** Summary seasonal modelled foehn frequency statistics for ice shelf and inlet stations on the Larsen C ice shelf over the period 1998-2017. Means, medians and standard deviations ("SD") are given for each season and annual totals. Values are calculated using the isentrope-based method described in section 2.3.

| | | **Mean** | **SD** |
|---|---|---|---|
| Ice shelf | DJF | 11.2% | 3.7% |
| | MAM | 12.1% | 3.9% |
| | JJA | 13.4% | 3.3% |
| | SON | 14.5% | 3.1% |
| | ANN | 12.7% | 2.4% |
| | | **Mean** | **SD** |
| Inlet | DJF | 15.4% | 4.0% |
| | MAM | 15.4% | 3.7% |
| | JJA | 16.1% | 3.0% |
| | SON | 18.5% | 2.7% |
| | ANN | 16.1% | 1.9% |

### 3.5 Frequency of foehn events: Larsen C, MAM 2016

Unusually frequent and intense foehn flow was simulated in the hindcast during the second half of MAM 2016 (Table 4), the period also examined in Kuipers Munneke et al. (2018). Only two years of observations were used in the Kuipers Munneke et al. study, which made it impossible to determine how anomalous these conditions were. However, the 20 years of hindcast data presented here make it possible to contextualise these findings.

Mean meteorological conditions during April 15 – May 31 2016 are shown in Figure 7a. Strong cross-peninsula flow is simulated and mean near-surface daily maximum air temperatures are 5.8°C warmer than climatology for the period, causing surface temperatures to frequently reach the melting point and for air temperatures to climb as high as 12.6°C in Mill Inlet on the 25 May 2016 (the peak of the case identified in Kuipers Munneke et al. (2018) as being strongest in the entire AWS 18 observational record).

This synoptic situation creates optimum conditions for foehn to occur. Panels b – f in Figure 7 show mean anomalies for individual SEB components during April 15 – May 31. Increased surface temperature produces modest negative $LW_{\uparrow}$ and $LW_{net}$ anomalies (Figure 7b) but the turbulent fluxes differ considerably from the climatology. Negative $H_L$ anomalies leeward of the

mountains (Figure 7c) indicate that the air is drier than the climatology and that sublimation occurs over Larsen C. Extremely positive sensible heat anomalies (Figure 7d) are modelled east of the mountain crest and extend across the ice shelf as foehn flow mixes warm, dry air towards the surface. This strong foehn effect generates mean $E_{tot}$ anomalies (Figure 7e) of up to 76.8 W $m^{-2}$ in the lee of the mountains. Mean $E_{melt}$ anomalies (Figure 7f) of up to 61.1 W $m^{-2}$ are simulated wherever $E_{tot}$ is positive, as mean maximum air temperatures are above 0°C in almost all locations (Figure 7a). These modelled anomalies agree well with the observational and model data presented in Kuipers Munneke et al. (2018), which show that foehn events produced by the isentropic drawdown mechanism (Elvidge & Renfrew, 2016) delivered large sensible heat fluxes (up to 300 W $m^{-2}$ in the strongest case) that were responsible for driving melting during May 2016.

**Table 4.** Mean modelled MAM foehn occurrence during the model hindcast period ("1998-2017 mean"), mean modelled MAM foehn occurrence during the hindcast period plus one standard deviation ("Mean + SD") and modelled foehn occurrence during MAM 2016 ("MAM 2016") at each station. As in Table 3, these values were computed using the isentropes-based method described in section 2.3.

| AWS | 1998-2017 mean (%) | Mean + SD (%) | MAM 2016 (%) |
|---|---|---|---|
| AWS 14 | 13.9 | 17.6 | 22.8 |
| AWS 15 | 10.3 | 13.5 | 18.3 |
| AWS 17 | 15.7 | 19.3 | 21.5 |
| AWS 18 | 15.1 | 18.9 | 24.2 |

Figure 8 shows that the associated $E_{melt}$ anomalies result in anomalous cumulative meltwater production over Larsen C, with 29 times more melt (5.7 Gt) produced during the MAM 2016 season than in the 1998-2017 MAM climatology (0.2 Gt), representing 35.4% of the meltwater production for the 2015/16 melt year (August-July, 16.0 Gt). This value is consistent with the 23% of annual meltwater production reported by Kuipers Munneke et al. (2018) for the period January-December 2016.

The mean modelled MAM 2016 meltwater production anomaly over Larsen C relative to the model MAM climatology is shown in Figure b, with maximum simulated melt along a transect shown in Figure 8a. Maximum melt fluxes along the transect are highest in the immediate lee of the mountains, and diminish rapidly with distance from the peak of orography as warm, dry foehn air is increasingly mixed into cold ambient air masses. Regions of elevated melt exist further out onto the ice shelf in some regions, with "streams" of higher melt emanating from the mouths of inlets. The locations of these qualitatively match with the foehn "jet" regions identified by Elvidge et al. (2015), which are typically cooler but experience higher wind speeds during foehn events. They are downstream of mountain passes which channel flow and enhance wind speeds, but cause air to be sourced from lower altitude, meaning that it is cooler when it reaches the surface than in adjacent "wake" regions. Because the events during MAM 2016 are so intense and ambient temperatures are so high, the relatively cooler jet temperatures do not limit melting, and the elevated wind speeds enhance the sensible heat flux enough to drive extremely intense melting in these jet regions.

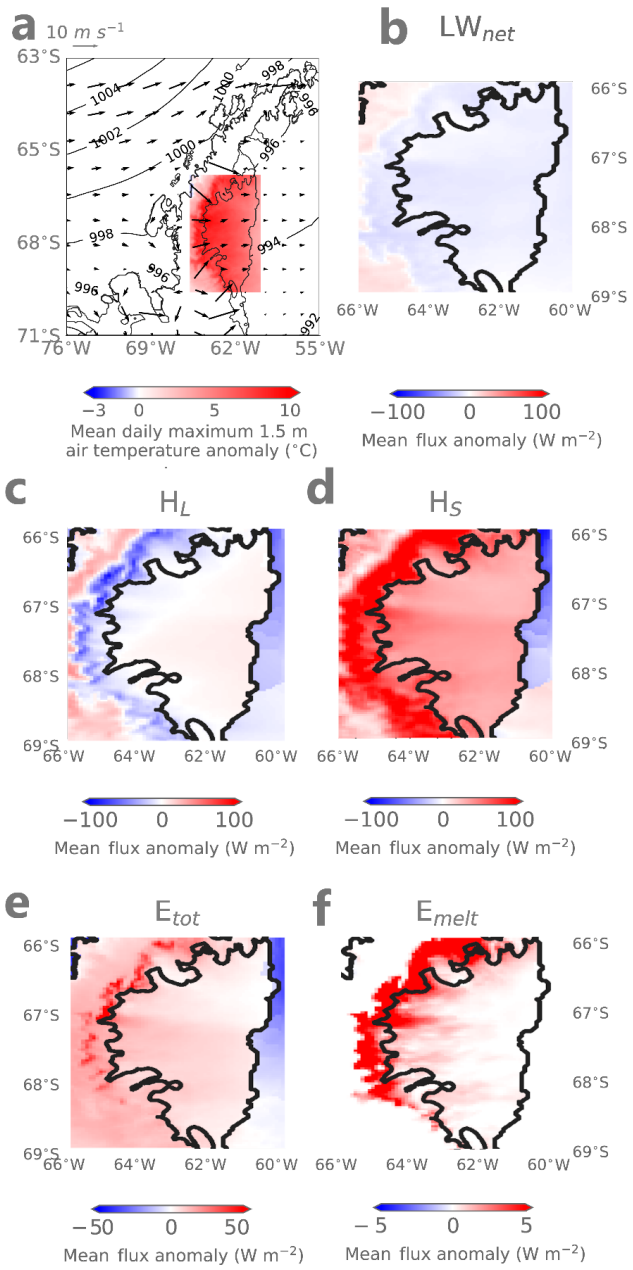


565 **Figure 7**. Mean modelled synoptic meteorological conditions and surface flux and temperature
566 anomalies during 15 April – 31 May 2016. Panel a) shows mean modelled meteorological
567 conditions, where colours indicate the mean daily maximum 1.5 m air temperature anomaly (in
568 °C), contours show mean sea level pressure (hPa) and vectors show mean 10 m wind speed and
569 direction. Panels b) to f) show flux anomalies, in W $m^{-2}$, of $LW_{net}$, $H_L$, $H_S$, $E_{tot}$ and $E_{melt}$,
570 respectively. In all panels the anomalies are calculated relative to the 1998-2017 model
571 climatology for 15 April – 31 May. Blue colours indicate negative anomalies while red colours
572 show positive anomalies.

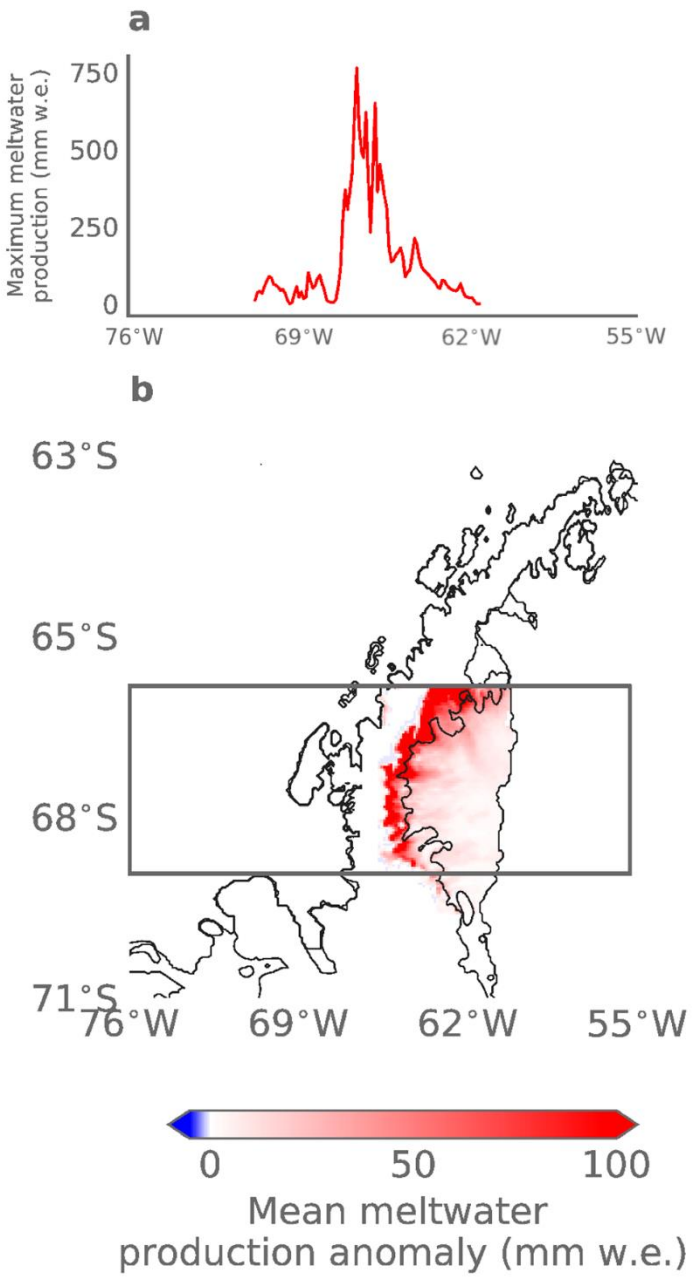


573

**Figure 8.** Mean meltwater production over Larsen C during 15 April – 31 May 2016. Panel a) shows the maximum cumulative melt produced along an east-west transect, indicated by the grey box in panel b). Panel b) shows the mean cumulative meltwater production anomaly with respect to the 1998-2017 model climatology for 15 April – 31 May.

574
575

## 5 Conclusions

The high-resolution regional model hindcast presented here is a novel dataset with which to evaluate meteorology, SEB and surface melt over the central Antarctic Peninsula. The hindcast reproduces the spatial patterns of surface melting on Larsen C identified from satellite observations, which are known to be linked to the incidence of foehn winds. This is the first multi-decadal hindcast of surface melt, meteorology and SEB to do so, and builds on Elvidge et al. (2020), which uses a similar configuration of the MetUM to explain the influence of foehn winds on the SEB of Larsen C during a shorter six-month period. Further, by re-visiting a case study of the period immediately preceding the collapse of the Larsen B ice shelf, we show that the hindcast captures both the magnitude of surface melting observed on Larsen B prior to its collapse, and that it reproduces the driving meteorological conditions implicated in its disintegration.

The long-term spatial distribution of foehn wind occurrence on Larsen C is mapped for the first time and closely matches the patterns of surface melting seen in satellite datasets, further implying a prominent role for foehn in driving melting. Compared to other years in the hindcast, much higher foehn frequency was simulated in MAM 2016, which was the subject of Kuipers Munneke et al. (2018). Exceptionally high foehn occurrence in this season (more than two standard deviations above the mean at three of the four AWSs considered) produced very large sensible heat flux anomalies, which drove positive $E_{tot}$ and $E_{melt}$ fluxes. These results indicate that the large proportion of melt, 23%, observed in the period April-October (taken to be 'winter' in Kuipers Munneke et al., 2018) was much higher in 2016 than it has been in other years in the hindcast.

Future work will further explore the causes and implications of surface melting on Larsen C. Part 2 of this study will use the hindcast model output to identify the most important meteorological drivers of surface melting on Larsen C, specifically by quantifying the influence of foehn winds, cloud phase and large-scale circulation on the SEB.

## Appendix

**Table A1.** Available output variables from the MetUM hindcast, including variable standard names, units, output frequency, vertical levels and availability. Full details of how to access the data are given in the data availability section of this paper.

| Standard name | Model units | Output time | Vertical levels | Availability |
|---|---|---|---|---|
| near-surface air temperature | K | 3 hr, inst. | 1.5 m | CEDA archive |
| surface temperature | K | 3 hr, inst. | surface | CEDA archive |
| surface pressure | Pa | 3 hr, inst. | surface | CEDA archive |
| mean sea level pressure | Pa | 3 hr, inst. | sea level | CEDA archive |
| near-surface relative humidity | % | 3 hr, inst. | 1.5 m | CEDA archive |
| near-surface wind speed | $m\ s^{-1}$ | 3 hr, inst. | 10 m | CEDA archive |
| u wind | $m\ s^{-1}$ | 3 hr, inst. | 10 m | CEDA archive |
| v wind | $m\ s^{-1}$ | 3 hr, inst. | 10 m | CEDA archive |
| Boundary layer thickness | m | 3 hr, inst. | surface | CEDA archive |
| surface altitude | m | one off | surface | CEDA archive |
| land sea mask | 1 | one off | surface | CEDA archive |
| sea ice area fraction | % | 3 hr, inst. | surface | CEDA archive |
| total cloud fraction | 1 | 3 hr, inst. | total column, integrated (single level) | CEDA archive |
| water vapour path | $kg\ m^{-2}$ | 3 hr, inst. | total column, integrated (single level) | CEDA archive |
| condensed water path | $kg\ m^{-2}$ | 3 hr, inst. | total column, integrated (single level) | CEDA archive |
| ice water path | $kg\ m^{-2}$ | 3 hr, inst. | total column, integrated (single level) | CEDA archive |
| cloud ice mass fraction (QCF) | $kg\ kg^{-1}$ | 6 hr, inst. | full profile | On request |
| cloud liquid mass | $kg\ kg^{-1}$ | 6 hr, inst. | full profile | On request |

| | | | | |
|---|---|---|---|---|
| fraction (QCL) | | | | |
| surface downwelling shortwave radiation | W $m^{-2}$ | 3 hr, inst. | surface | CEDA archive |
| surface downwelling longwave radiation | W $m^{-2}$ | 3 hr, inst. | surface | CEDA archive |
| surface upward latent heat flux | W $m^{-2}$ | 3 hr, inst. | surface | CEDA archive |
| surface upward sensible heat flux | W $m^{-2}$ | 3 hr, inst. | surface | CEDA archive |
| surface net shortwave radiation | W $m^{-2}$ | 3 hr, inst. | surface | CEDA archive |
| surface net longwave radiation | W $m^{-2}$ | 3 hr, inst. | surface | CEDA archive |
| TOA outgoing longwave radiation | W $m^{-2}$ | 3 hr, inst. | TOA | CEDA archive |
| TOA incident shorwave radiation | W $m^{-2}$ | 3 hr, inst. | TOA | CEDA archive |
| TOA outgoing shortwave radiation | W $m^{-2}$ | 3 hr, inst. | TOA | CEDA archive |
| land snow melt amount | kg $m^{-2}$ | 3 hr, inst. | surface | CEDA archive |
| land snow melt flux | W $m^{-2}$ | 3 hr, inst. | surface | CEDA archive |
| potential temperature | K | 6 hr, inst. | Full profile | On request |
| specific humidity | kg $kg^{-1}$ | 6 hr, inst. | Full profile | On request |
| air temperature | K | 6 hr, inst. | Pressure level set: 1000, 950,850,700, 625, 500, | CEDA archive |

| | | | | |
|---|---|---|---|---|
| | | | 300, 200 hPa | |
| | | | Pressure level set: 1000, | |
| | m $s^{-1}$ | 6 hr, inst. | 950,850,700, 625, 500, | CEDA archive |
| eastward wind | | | 300, 200 hPa | |
| | | | Pressure level set: 1000, | |
| | m $s^{-1}$ | 6 hr, inst. | 950,850,700, 625, 500, | CEDA archive |
| northward wind | | | 300, 200 hPa | |

Abbreviations are as follows. TOA: top-of-atmosphere; 3 hr, inst.: 3 hourly, instantaneous output; CEDA: Centre for Environmental Data Analysis. See data availability section for more information.

612

613

## 614 Acknowledgments, Samples, and Data

615 The authors declare no conflicts of interest. This work was supported by the Natural
616 Environment Research Council through the EnvEast Doctoral Training Partnership (grant
617 number NE/L002582/1). The authors also acknowledge use of the MONSooN system, a
618 collaborative facility supplied under the Joint Weather and Climate Research Programme, a
619 strategic partnership between the Met Office and the Natural Environment Research Council.
620 The authors gratefully acknowledge Prof. Michiel R. van den Broeke, who kindly provided AWS
621 data.

622 Hindcast model data can be accessed on the CEDA archive at
623 https://catalogue.ceda.ac.uk/uuid/41c879b06af642e9bc8e12d1d0ea3d62 and can be cited as
624 Gilbert, E. (2020): High-resolution regional Met Office Unified Model (UM) climate model
625 hindcast of the Antarctic Peninsula (1998-2017). Centre for Environmental Data Analysis, date
626 of citation. AWS data can be retrieved from https://www.projects.science.uu.nl/iceclimate/aws/.

## References


Bevan, S., Luckman, A., Hubbard, B., Kulessa, B., Ashmore, D., Kuipers Munneke, P., O'Leary, M., Booth, A., Sevestre, H., & McGrath, D. (2017). Centuries of intense surface melt on Larsen C Ice Shelf. *The Cryosphere Discussions*, 1–21. https://doi.org/10.5194/tc-2017-81

Borstad, C. P., Rignot, E., Mouginot, J., & Schodlok, M. P. (2013). Creep deformation and buttressing capacity of damaged ice shelves: Theory and application to Larsen C ice shelf. *Cryosphere*, *7*(6), 1931–1947. https://doi.org/10.5194/tc-7-1931-2013

Bush, M., Allen, T., Bain, C., Boutle, I., Edwards, J., Finnenkoetter, A., Franklin, C., Hanley, K., Lean, H., Lock, A., Manners, J., Mittermaier, M., Morcrette, C., North, R., Petch, J., Short, C., Vosper, S., Walters, D., Webster, S., … Zerroukat, M. (2020). The first Met Office Unified Model-JULES Regional Atmosphere and Land configuration, RAL1. *Geoscientific Model Development*, *13*, 1999–2029. https://doi.org/10.5194/gmd-13-1999-2020

Cape, M. R., Vernet, M., Skvarca, P., Marinsek, S., Scambos, T., & Domack, E. (2015). Foehn winds link climate-driven warming to ice shelf evolution in Antarctica. *Journal of Geophysical Research: Atmospheres*, *120*(21), 11037–11057. https://doi.org/10.1002/2015JD023465

Cook, A. J., & Vaughan, D. G. (2010). Overview of areal changes of the ice shelves on the Antarctic Peninsula over the past 50 years. *The Cryosphere Discussions*, *3*(2), 579–630. https://doi.org/10.5194/tcd-3-579-2009

Datta, R. T., Tedesco, M., Fettweis, X., Agosta, C., Lhermitte, S., Lenaerts, J. T. M., & Wever, N. (2019). The Effect of Foehn-Induced Surface Melt on Firn Evolution Over the Northeast Antarctic Peninsula. *Geophysical Research Letters*, *46*, 3822–3831. https://doi.org/10.1029/2018GL080845

Dee, D. P., Uppala, S. M., Simmons, A. J., Berrisford, P., Poli, P., Kobayashi, S., Andrae, U., Balmaseda, M. A., Balsamo, G., Bauer, P., Bechtold, P., Beljaars, A. C. M., van de Berg, L., Bidlot, J., Bormann, N., Delsol, C., Dragani, R., Fuentes, M., Geer, A. J., … Vitart, F. (2011). The ERA-Interim reanalysis: Configuration and performance of the data assimilation system.

Q*uarterly Journal of the Royal Meteorological Society*, *137*(656), 553–597. https://doi.org/10.1002/qj.828

Dutra, E., Sandu, I., Balsamo, G., Beljaars, A., Freville, H., Vignon, E., & Brun, E. (2015). Understanding the ECMWF winter surface temperature biases over Antarctica. In *ECMWF Internal Report* (Vol. 762, Issue January 2016). https://doi.org/10.13140/RG.2.1.5165.5762

Elvidge, A. D., & Renfrew, I. A. (2016). The causes of foehn warming in the lee of mountains. *Bulletin of the American Meteorological Society*, *97*(3), 455–466. https://doi.org/10.1175/BAMS-D-14-00194.1

Elvidge, A. D., Renfrew, I. A., King, J. C., Orr, A., Lachlan-Cope, T. A., Weeks, M., & Gray, S. L. (2015). Foehn jets over the Larsen C Ice Shelf, Antarctica. *Quarterly Journal of the Royal Meteorological Society*, *141*(688), 698–713. https://doi.org/10.1002/qj.2382

Elvidge, A. D., Renfrew, I. A., King, J. C., Orr, A., & Lachlan-Cope, T. A. (2016). Foehn warming distributions in nonlinear and linear flow regimes: A focus on the Antarctic Peninsula. *Quarterly Journal of the Royal Meteorological Society*, *142*(695), 618–631. https://doi.org/10.1002/qj.2489

Elvidge, A. D., Kuipers Munneke, P., King, J. C., Renfrew, I. A., & Gilbert, E. (2020). Atmospheric Drivers of Melt on Larsen C Ice Shelf: Surface Energy Budget Regimes and the Impact of Foehn. *Journal of Geophysical Research: Atmospheres*, *125*(17). https://doi.org/10.1029/2020JD032463

Fréville, H., Brun, E., Picard, G., Tatarinova, N., Arnaud, L., Lanconelli, C., Reijmer, C., & Van Den Broeke, M. (2014). Using MODIS land surface temperatures and the Crocus snow model to understand the warm bias of ERA-Interim reanalyses at the surface in Antarctica. *Cryosphere*, *8*(4), 1361–1373. https://doi.org/10.5194/tc-8-1361-2014

Fürst, J. J., Durand, G., Gillet-chaulet, F., Tavard, L., Rankl, M., Braun, M., & Gagliardini, O. (2016). The safety band of Antarctic ice shelves. *Nature Climate Change*, *6*(February), 2014–2017. https://doi.org/10.1038/NCLIMATE2912

679 Gilbert, E. (2020) Atmospheric drivers of surface melting on the Larsen C ice shelf, Antarctic
680 Peninsula. PhD thesis, University of East Anglia.

681 Gilbert, E., Orr, A., King, J. C., Renfrew, I. A., Lachlan-Cope, T., Field, P. F., & Boutle, I. A.
682 (2020). Summertime cloud phase strongly influences surface melting on the Larsen C ice shelf,
683 Antarctica. *Quarterly Journal of the Royal Meteorological Society*, *146*(729), 1575–1589.
684 https://doi.org/10.1002/qj.3753

685 Holland, P. R., Corr, H. F. J., Pritchard, H. D., Vaughan, D. G., Arthern, R. J., Jenkins, A., &
686 Tedesco, M. (2011). The air content of Larsen Ice Shelf. *Geophysical Research Letters*, *38*(10),
687 1–6. https://doi.org/10.1029/2011GL047245

688 Hubbard, B., Luckman, A., Ashmore, D. W., Bevan, S., Kulessa, B., Kuipers Munneke, P.,
689 Philippe, M., Jansen, D., Booth, A., Sevestre, H., Tison, J.-L., O'Leary, M., & Rutt, I. (2016).
690 Massive subsurface ice formed by refreezing of ice-shelf melt ponds. *Nature Communications*,
691 *7*(May), 11897. https://doi.org/10.1038/ncomms11897

692 Khazendar, A., Rignot, E., & Larour, E. (2011). Acceleration and spatial rheology of Larsen C
693 Ice Shelf , Antarctic Peninsula. *Geophysical Research Letters*, *38*(January), 1–5.
694 https://doi.org/10.1029/2011GL046775

695 King, J. C., Kirchgaessner, A., Orr, A., Luckman, A., Bevan, S., Elvidge, A., Renfrew, I. A., &
696 Kuipers Munneke, P. (2017). The impact of foehn winds on surface energy balance and melt
697 over Larsen C Ice Shelf, Antarctica. *Journal of Geophysical Research: Atmospheres*, *122*(22),
698 12062–12076. https://doi.org/10.1002/2017JD026809

699 Kirchgaessner, A., King, J., & Gadian, A. (2019). The Representation of Föhn Events to the East
700 of the Antarctic Peninsula in Simulations by the Antarctic Mesoscale Prediction System. *Journal*
701 *of Geophysical Research: Atmospheres*, *124*(24), 13663–13679.
702 https://doi.org/10.1029/2019JD030637

703 Kuipers Munneke, P., Ligtenberg, S. R. M., Van Den Broeke, M. R., & Vaughan, D. G. (2014).
704 Firn air depletion as a precursor of Antarctic ice-shelf collapse. *Journal of Glaciology*, *60*(220),
705 205–214. https://doi.org/10.3189/2014JoG13J183

Kuipers Munneke, P., Van Den Broeke, M. R., King, J. C., Gray, T., & Reijmer, C. H. (2012). Near-surface climate and surface energy budget of Larsen C ice shelf, Antarctic Peninsula. *Cryosphere*, *6*(2), 353–363. https://doi.org/10.5194/tc-6-353-2012

Kuipers Munneke, P., van den Broeke, M. R., Reijmer, C. H., Helsen, M. M., Boot, W., Schneebeli, M., & Steffen, K. (2009). The role of radiation penetration in the energy budget of the snowpack at Summit, Greenland. *The Cryosphere*, *3*(1), 155–165. https://doi.org/10.5194/tcd-3-277-2009

Liu, H., Jezek, K. C., Li, B., & Zhao, Z. (2015). *RadarSat Antarctic Mapping Project Digital Elevation Model, version 2*. NSIDC; NASA National Snow and Ice Data Center Distributed Active Archive Center. https://doi.org/https://doi.org/10.5067/8JKNEW6BFRVD

Luckman, A., Elvidge, A., Jansen, D., Kulessa, B., Kuipers Munneke, P., King, J., & Barrand, N. E. (2014). Surface melt and ponding on Larsen C Ice Shelf and the impact of föhn winds. *Antarctic Science*, *26*(6), 625–635. https://doi.org/10.1017/S0954102014000339

Orr, A., Hunt, J. C. R., Capon, R., Sommeria, J., Cresswell, D., & Owinoh, A. (2005). Coriolis effects on wind jets and cloudiness along coasts. *Weather*, *60*(10), 291–299.

Orr, A., Phillips, T., Webster, S., Elvidge, A., Weeks, M., Hosking, S., & Turner, J. (2014). Met Office Unified Model high-resolution simulations of a strong wind event in Antarctica. *Quarterly Journal of the Royal Meteorological Society*, *140*(684), 2287–2297. https://doi.org/10.1002/qj.2296

Parish, T. R. (1983). The Influence of the Antarctic Peninsula on the Wind Field Over the Western Weddell Sea. Journal of Geophysical Research, 88(C4), 2684–2692. https://doi.org/10.1029/JC088iC04p02684

Rignot, E., Casassa, G., Gogineni, P., Krabill, W., Rivera, A., & Thomas, R. (2004). Accelerated ice discharge from the Antarctic Peninsula following the collapse of Larsen B ice shelf. *Geophysical Research Letters*, *31*(July), 2–5. https://doi.org/10.1029/2004GL020697

Rott, H., Rack, W., Skvarca, P., & De Angelis, H. (2002). Northern Larsen Ice Shelf, Antarctica: further retreat after collapse. *Annals of Glaciology*, *34*, 277–282. https://doi.org/https://doi.org/10.3189/172756402781817716

Rott, H., Skvarca, P., & Nagler, T. (1996). Rapid collapse of Northern Larsen ice shelf, Antarctica. *Science*, *271*(5250), 788–792. https://doi.org/10.1126/science.271.5250.788

Scambos, T. A., Bohlander, J. A., Shuman, C. A., & Skvarca, P. (2004). Glacier acceleration and thinning after ice shelf collapse in the Larsen B embayment, Antarctica. *Geophysical Research Letters*, *31*(18), 2001–2004. https://doi.org/10.1029/2004GL020670

Scambos, T. A., Hulbe, C., & Fahnestock, M. (2003). Climate-induced ice shelf disintegration in the Antarctic Peninsula. In E. Domack, A. Leventer, A. Burnet, R. Bindschadler, P. Convey, & M. Kirby (Eds.), *Antarctic Peninsula Climate Variability: Historical and Paleoenvironmental Perspectives* (Vol. 79, pp. 79–92). American Geophysical Union. https://doi.org/doi:10.1029/AR079p0079

Scambos, T. A., Hulbe, C., M.Fahnestock, & J.Bohlander. (2000). The link between climate warming and break-up of ice shelves in the Antarctica Peninsula. *Journal of Glaciology*, *46*(154), 516–530. https://doi.org/http://dx.doi.org/10.3189/172756500781833043

Sedlar, J., Tjernström, M., Rinke, A., Orr, A., Cassano, J., Fettweis, X., Heinemann, G., Seefeldt, M., Solomon, A., Matthes, H., Phillips, T., & Webster, S. (2020). Confronting Arctic Troposphere, Clouds, and Surface Energy Budget Representations in Regional Climate Models With Observations. *Journal of Geophysical Research: Atmospheres*, *125*(6), 1–29. https://doi.org/10.1029/2019JD031783

Smeets, C. J. P. P. (2006). Assessing unaspirated temperature measurements using a thermocouple and a physically based model. The Mass Budget of Arctic Glaciers. Extended Abstracts, Workshop and GLACIODYN Planning Meeting, 29, 99–101. Available online at: https://webspace.science.uu.nl/~reijm101/publications/2006_abstracts_nag.pdf#page=100

Smeets, P. C. J. P., Kuipers Munneke, P., van As, D., van den Broeke, M. R., Boot, W., Oerlemans, H., Snellen, H., Reijmer, C. H., & van de Wal, R. S. W. (2018). The K-transect in

west Greenland: Automatic weather station data (1993–2016). *Arctic, Antarctic, and Alpine Research*, *50*(1), e1420954. https://doi.org/10.1080/15230430.2017.1420954

Trusel, L. D., Frey, K. E., Das, S. B., Karnauskas, K. B., Kuipers Munneke, P., van Meijgaard, E., & van den Broeke, M. R. (2015). Divergent trajectories of Antarctic surface melt under two twenty-first-century climate scenarios. *Nature Geoscience*, *8*(12), 927–932. https://doi.org/10.1038/ngeo2563

Trusel, L. D., Frey, K. E., Das, S. B., Kuipers Munneke, P., & Van Den Broeke, M. R. (2013). Satellite-based estimates of Antarctic surface meltwater fluxes. *Geophysical Research Letters*, *40*(23), 6148–6153. https://doi.org/10.1002/2013GL058138

Turner, J., Lu, H., White, I., King, J. C., Phillips, T., Hosking, J. S., Bracegirdle, T. J., Marshall, G. J., Mulvaney, R., & Deb, P. (2016). Absence of 21st century warming on Antarctic Peninsula consistent with natural variability. Nature, 535(7612), 411–415. https://doi.org/10.1038/nature18645

Turton, J. V., Kirchgaessner, A., Ross, A. N., & King, J. C. (2018). The spatial distribution and temporal variability of föhn winds over the Larsen C ice shelf, Antarctica. *Quarterly Journal of the Royal Meteorological Society*, *144*(713), 1169–1178. https://doi.org/10.1002/qj.3284

van den Broeke, M. (2005). Strong surface melting preceded collapse of Antarctic Peninsula ice shelf. *Geophysical Research Letters*, *32*, 2–5. https://doi.org/10.1029/2005GL023247

Van Wessem, J. M., Ligtenberg, S. R. M., Reijmer, C. H., Van De Berg, W. J., Van Den Broeke, M. R., Barrand, N. E., Thomas, E. R., Turner, J., Wuite, J., Scambos, T. A., & Van Meijgaard, E. (2016). The modelled surface mass balance of the Antarctic Peninsula at 5.5 km horizontal resolution. *Cryosphere*, *10*(1), 271–285. https://doi.org/10.5194/tc-10-271-2016

Van Wessem, J. M., Reijmer, C. H., Van De Berg, W. J., Van Den Broeke, M. R., Cook, A. J., Van Ulft, L. H., & Van Meijgaard, E. (2015). Temperature and wind climate of the Antarctic Peninsula as simulated by a high-resolution Regional Atmospheric Climate Model. *Journal of Climate*, *28*(18), 7306–7326. https://doi.org/10.1175/JCLI-D-15-0060.1

Walters, D., Boutle, I., Brooks, M., Melvin, T., Stratton, R., Vosper, S., Wells, H., Williams, K., Wood, N., Allen, T., Bushell, A., Copsey, D., Earnshaw, P., Edwards, J., Gross, M., Hardiman, S., Harris, C., Heming, J., Klingaman, N., … Xavier, P. (2017). The Met Office Unified Model Global Atmosphere 6.0/6.1 and JULES Global Land 6.0/6.1 configurations. *Geoscientific Model Development*, *10*(4), 1487–1520. https://doi.org/10.5194/gmd-10-1487-2017

Wang, W., Zender, C. S., Van As, D., Smeets, P. C. J. P., & Van Den Broeke, M. R. (2016). A Retrospective, Iterative, Geometry-Based (RIGB) tilt-correction method for radiation observed by automatic weather stations on snow-covered surfaces: Application to Greenland. *Cryosphere*, *10*(2), 727–741. https://doi.org/10.5194/tc-10-727-2016

Wiesenekker, J. M., Kuipers Munneke, P., van den Broeke, M. R., & Smeets, P. C. J. P. (2018). A multidecadal analysis of Föhn winds over Larsen C ice shelf from a combination of observations and modeling. *Atmosphere*, *9*(5). https://doi.org/10.3390/atmos9050172

Wood, N., & Mason, P. (1993). The Pressure force induced by neutral, turbulent flow over hills. *Quarterly Journal of the Royal Meteorological Society*, *119*(514), 1233–1267. https://doi.org/10.1002/qj.49711951402

Wood, N., Staniforth, A., White, A., Allen, T., Diamantakis, M., Gross, M., Melvin, T., Smith, C., Vosper, S., Zerroukat, M., & Thuburn, J. (2014). An inherently mass-conserving semi-implicit semi-Lagrangian discretization of the deep-atmosphere global non-hydrostatic equations. *Quarterly Journal of the Royal Meteorological Society*, *140*(682), 1505–1520. https://doi.org/10.1002/qj.2235